A pH-Responsive Persistent Luminescence Nanozyme for Selective Imaging and Killing of *Helicobacter pylori* and Common Resistant Bacteria

Li-Xia Yan, Bei-Bei Wang, Xu Zhao, Li-Jian Chen, and Xiu-Ping Yan*

Cite This: *ACS Appl. Mater. Interfaces* 2021, 13, 60955−60965

Read Online

ACCESS | Metrics & More | Article Recommendations | Supporting Information

ABSTRACT: *Helicobacter pylori* (*H. pylori*) infection is implicated in the etiology of many diseases. *H. pylori* eradication by antibiotic therapy is limited by the extreme acidic environment in the stomach, the undesired side effect of intestinal commensal bacteria, and the development of drug resistance. Here, we report a pH-responsive persistent luminescence (PL) nanozyme (MSPLNP-Au-CB) for in vivo imaging and inactivation of *H. pylori*. This PL nanozyme is composed of mesoporous silica (MS)-coated persistent luminescence nanoparticles (MSPLNP), Au nanoparticles (AuNP), and chitosan-benzeneboronic acid (CB), taking advantage of the long PL of PLNP to realize autofluorescence-free imaging, the pH-activated oxidase- and peroxidase-like nanozyme activity of AuNP, and the bacterial binding capacity of CB. The MSPLNP-Au-CB nanozyme can resist the corrosion of gastric acid and exhibit pH-activated dual nanozyme activity to catalyze bactericidal reactive oxygen species generation. This multifunctional nanozyme enables targeted imaging and activated deactivation of *H. pylori* under extreme gastric acid conditions as well as methicillin-resistant *Staphylococcus aureus* in common slightly acidic environments, while it has no side effects on the commensal bacteria and normal cells in normal physiological environments. This work provides a promising PL nanozyme platform for bioimaging and therapy of bacterial infection under harsh conditions.

KEYWORDS: *Helicobacter pylori*, pH-responsive, persistent luminescence, nanozyme, antibacterial effect
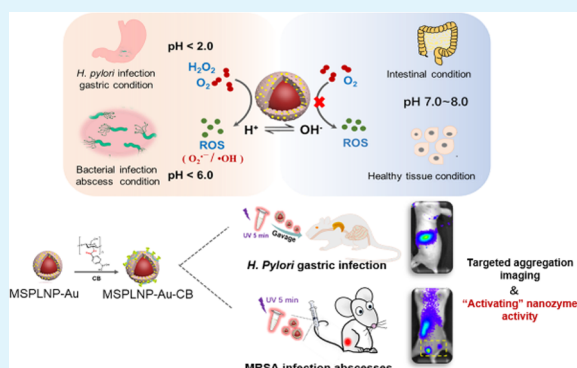
INTRODUCTION

Helicobacter pylori (*H. pylori*), a bacterium with a pronounced capability of adaptation under extreme environmental stress conditions, is responsible for life threatening infections, for instance, peptic ulcer, gastric ulcers, and even gastric cancer.[1−4] *H. pylori* infection is one of the widespread and most persistent bacterial infections with approximately half of the world's population infected. Moreover, *H. pylori*-induced injury and inflammation account for approximately 75% of gastric cancer cases.[5] *H. pylori* is classified as a type I carcinogen by the International Agency for Cancer Research.[6] In fact, *H. pylori* is the only bacterium classified as a Class I carcinogen.[7] Given its potential for crucial comorbidity, appropriate and effective therapy is indispensable to prevent future complications.[8]

Clarithromycin triple therapy consisting of a proton pump inhibitor (omeprazole) and two antibiotics (amoxicillin and clarithromycin/metronidazole) is the standard first-line therapy.[9,10] However, such a triple therapy is greatly challenged by the undesired killing of commensal bacteria due to its poor selectivity and development of drug resistance.[11,12] The World Health Organization includes *H. pylori* on the "high-priority" list of antibiotic-resistant bacteria.[13] In addition, the gastric milieu with strong acidity poses a dilemma for *H. pylori*

eradication. To solve these issues, it is necessary to develop a selective method with minimum antibiotic resistance for killing *H. pylori* in the stomach.

Nanozymes are new emerging "antibiotics" with broad-spectrum sterilization potency. Versatile nanozymes have been uncovered up to date, such as metal nanomaterials,[14−17] metal oxides/sulfides,[18−24] metal−organic frameworks,[25−28] and carbon-based nanomaterials.[29−31] These nanozymes exhibit excellent antibacterial activity by generating reactive oxygen species (ROS) to destroy the membranes of bacteria via oxidization. Most of the nanozymes are generally used to inactivate bacteria under wound infection conditions. However, there are relatively few nanozymes for killing bacteria in specific extreme environments, such as *H. pylori* in a strongly acidic stomach.[32] In this case, the nanozymes should not only
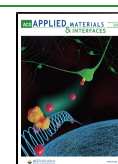
resist the gastric acid corrosion but also still possess inherent enzyme-like activity under strong acidic conditions. In addition, for in vivo applications, nanozymes are in general toxic to bacteria, mammalian cells, and intestinal commensal bacteria, with lack of selectivity as ideal antimicrobials. Thus, target site-directed activation of nanozymes should be considered to improve the therapeutic efficacy with simultaneous reduction of side effects against mammalian cells, symbiotic probiotics, and the uninfected sites.

Nanozymes normally exhibit peroxidase-like activity under acidic conditions (pHs 3−6) by preabsorption of H^{+} and base-like decomposition of H_2O_2 to ROS in antibacterial application.[33−35] However, physiological H_2O_2 is inadequate to realize efficient chemodynamic therapy.[36] Therefore, nanozymes with oxidase-mimicking activity are needed for efficient antibacterial application.[37] Moreover, a single-modal antibacterial process of nanozymes is unable to realize effective antibacterial activity. For these reasons, a visualized nanoplatform is necessary for the timely imaging of bacterial infection and real-time monitoring of the therapy process.

Persistent luminescence nanoparticles (PLNP) are promising optical materials with long-lasting luminescence after excitation light is removed, allowing autofluorescence-free persistent luminescence imaging without the need for constant in situ excitation.[38−40] Cr^{3+}-doped near-infrared (NIR) emitting PLNP possess an additional advantage of renewability with tissue-penetrating red LED light, making PLNP-based luminescence imaging no longer subjected to afterglow time.[41,42] Therefore, Cr^{3+}-doped NIR-emitting PLNP are ideal to build a visualized nanoplatform for autofluorescence-free and long-term monitoring bioapplication.

Herein, we report a persistent luminescence (PL) nanozyme with remarkable pH-activated oxidase- and peroxidase-like activities for selective killing of H. pylori along with autofluorescence-free luminescence imaging for real-time monitoring of therapy. Cr^{3+}-doped zinc gallogermanate nanoparticles (PLNP) ($Zn_{1.2}Ga_{1.6}Ge_{0.2}O_4{:}Cr^{3+}$) are used as the core of this nanozyme due to their NIR-emitting persistent luminescence.[38] Expanded mesoporous silica (MS) is in situ formed on the surface of the PLNP to obtain MS-coated PLNP (MSPLNP) with rich channels for hosting gold nanoparticles (AuNP). AuNP are then in situ grown on the abundant channels of MSPLNP to get core−shell MSPLNP-Au with dual nanozyme activity. Further functionalization with chitosan-benzeneboronic acid (CB) gives the PL nanozyme MSPLNP-Au-CB for bacterial targeting. The obtained MSPLNP-Au-CB integrates the merits of the red LED light-renewable long PL, pH-activated oxidase/peroxidase-like activity, and selective bacterial targeting capability. This PL nanozyme provides targeted luminescence imaging and effective pH-responsive bacterial inactivation toward H. pylori in gastric acid conditions and methicillin-resistant Staphylococcus aureus (MRSA) in bacterial infection common acidic conditions but has a negligible harmful effect on intestinal symbiotic bacteria and normal cells.

■ RESULTS AND DISCUSSION

Design, Preparation, and Characterization of MSPLNP-Au. Scheme 1a shows the design of the MSPLNP-Au nanozyme. The PLNP synthesized via a solvothermal approach with further sintering[43] were used as the core of the nanoplatform to achieve autofluorescence-free bioimaging with long-lasting and red-light reversible reactivated NIR persistent

Scheme 1. Preparation and Illustration of MSPLNP-Au: (a) Schematic for the Design and Preparation of MSPLNP-Au and (b) Illustration of the pH-Responsive Oxidase- and Peroxidase-like Activity of MSPLNP-Au under Gastric Acid Conditions and Abscess Conditions
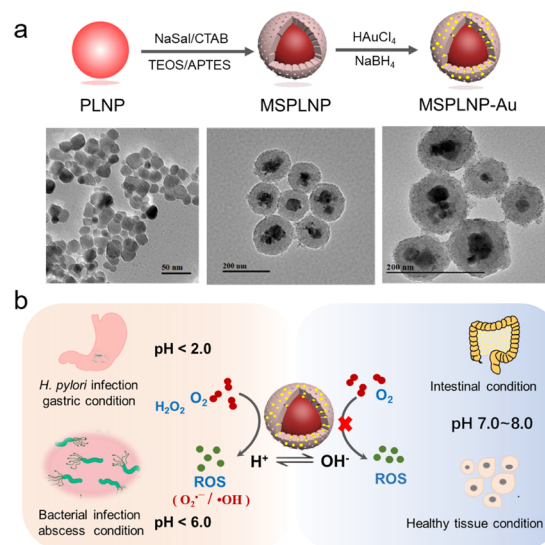
luminescence. The MS shell was formed on the PLNP surface via cocondensation with TEOS and APTES as silica and organo-silica precursors[44] to improve the bioavailability of the PLNP and provide sufficient channels for AuNP immobilization. The AuNP were immobilized on the channels of MSPLNP by forming N−Au covalent bonds with auric chloride ions and subsequent in situ reduction with NaBH$_4$[14] to get MSPLNP-Au with dual artificial enzyme activity. Meanwhile, the MS shell could serve as the solid support to protect "naked" AuNP from aggregation and keep the catalyst active and stable even under harsh conditions.

Scheme 1b illustrates the pH-responsive oxidase- and peroxidase-like activity of MSPLNP-Au under gastric acid conditions and abscess conditions. MSPLNP-Au would exhibit intrinsic oxidase- and peroxidase-like activity under gastric acid conditions or abscess acid conditions to catalyze ROS generation and attack the bacterial membrane. However, the nanozyme activity of MSPLNP-Au would be blocked under neutral intestinal or healthy tissue conditions, leading to a negligible harmful effect. Thus, the developed MSPLNP-Au allows the pH-responsive in vivo activation of nanozyme activity to kill bacteria.

The NIR-emitting PLNP core gave an average size of 20.7 ± 2.8 nm (N = 100) (Figure S1a,b) with pure cubic spinel structures of $ZnGa_2O_4$ (JCPDS 38-1240) and Zn_2GeO_4 (JCPDS 25-1018) (Figure S1c). The PLNP solution (0.5 mg mL^{-1}) gave a 700 nm NIR emission peak under 254 nm excitation (Figure S1d). The photoluminescence quantum yield of the PLNP was 33.1%. The PL signal of the PLNP could be easily captured and reactivated by red LED light (Figure S2), making it appropriate for autofluorescence-free long-term and real-time imaging in vivo.

The as-prepared MSPLNP exhibited an excellent core−shell structure with open pores and functional −NH$_2$ groups (Figure S3a) and gave the characteristic XRD peaks of the PLNP (Figure S3b) as well as those of MS with a well-ordered porous structure (a wide peak near 22° and a low-angle characteristic peak near 2.8°) (Figure S3b,c). Compared with

the PLNP core, MSPLNP gave a well-defined pore size (6.4 nm) with a larger BET surface area (670 m^2 g^{-1}) and pore volume (1.845 cc g^{-1}), providing abundant channels for AuNP loading (Figure S3d,e).

The FT-IR spectra (Figure S3f) show strong absorption bands at 1065, 959, and 795 cm^{-1} for Si−O−Si (antisymmetric stretching vibration), Si−OH (bending vibration), and Si−O bonds (symmetrical stretching vibration), respectively, confirming the formation of the MS shell. The characteristic peaks of N−H at 1566 cm^{-1} (bending vibration) as well as −CH$_2$− at 2921 and 2850 cm^{-1} (symmetrical and asymmetrical stretching vibrations) confirm the functional −NH$_2$ groups on MSPLNP.

TEM images (Figure 1a,b) and SEM images (Figure 1c) show that AuNP immobilized on MS were well-dispersed, with
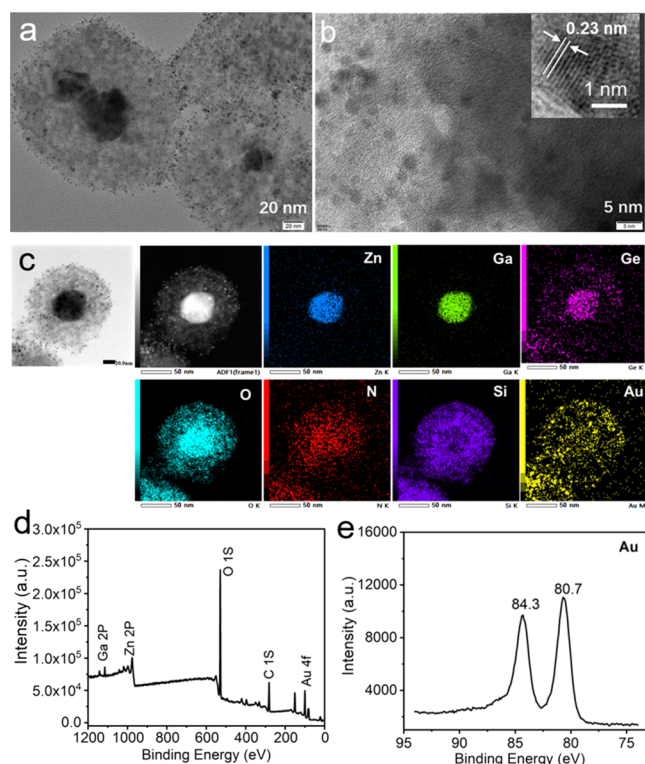

Figure 1. Characterization of MSPLNP-Au. (a) TEM image. (b) High-resolution TEM images. (c) EDS element mapping. (d) XPS spectra. (e) XPS spectra for Au 4f.

a size of about 2.0 ± 0.5 nm. The lattice plane distance was about 0.23 nm on average, corresponding to the lattice spacing of Au(111) planes (inset of Figure 1b). Meanwhile, the elements Zn, Ga, Ge, and O mainly appeared in the PLNP core, while the elements Si, O, N, and Au were uniformly presented in MSPLNP, suggesting the success of the immobilization of AuNP on MSPLNP (Figure 1c). The Au 4f peaks at 80.7 and 84.3 eV in the X-ray photoelectron spectra (XPS) also show the successful modification of AuNP on the MSPLNP surface (Figure 1d,e). The as-prepared MSPLNP-Au still maintained the easily reactivatable PL property as the PLNP core (Figure S4a,b), indicating the potential of MSPLNP-Au for in vivo imaging applications.

The stability of MSPLNP was examined as it would directly influence the nanozyme activity in gastric acid conditions. Time-dependent analysis of the hydrodynamic

diameter shows that MSPLNP-Au was stable in a simulated gastric fluid (SGF)[45] over 24 h (Figure S5a). The morphology and PL performance of MSPLNP-Au did not change after dispersing in the SGF for 24 h (Figure S5b,c). All the above results indicate the good stability of MSPLNP-Au in the SGF, making it suitable for long-term treatment and imaging in extreme acidic conditions of the stomach.

The oxidase-like activity of MSPLNP-Au was investigated with 3,3′,5,5′-tetramethylbenzidine (TMB) as a substrate. Figure 2a shows MSPLNP-Au for the catalytic oxidation of TMB (colorless) to oxTMB (deep blue color with major absorption peaks at 370 and 652 nm[46]). In contrast, MSPLNP did not produce a significant color change, confirming that the oxidase-like activity came from the intrinsic catalytic property of AuNP supported on MSPLNP. The oxidase-like activity of MSPLNP-Au was further revealed with other substrates. MSPLNP-Au could also catalyze the oxidation of both 2,2′-azino-bis (3-ethylbenzthiazoline-6-sulfonic acid) (ABTS) and o-phenylenediamine (OPD) as indicated from the UV−vis spectra and characteristic color changes (Figure 2b). Furthermore, the oxidase-like activity of MSPLNP-Au was systematically evaluated under various conditions (different reaction times, temperatures, and solution pHs) (Figures S6 and S7). The MSPLNP-Au nanozyme exhibited a pH-dependent oxidase-like property. It is noteworthy that MSPLNP-Au still maintained its intrinsic oxidase-like activity (about 76% at pH 1.0 compared to that at pH 3.0) even under extreme acidic conditions (Figure 2c).

The peroxidase-like activity of MSPLNP-Au was further evaluated by catalyzing various substrates (TMB, ABTS, and OPD) in the presence of H$_2$O$_2$ (Figure S8a) under different conditions (different reaction times, temperatures, and solution pHs) (Figure S8b−d). All of the results indicate the intrinsic oxidase/peroxidase-like activity of the as-prepared MSPLNP-Au, even under extreme acidic conditions, giving it potential for bioapplications at special gastric acid conditions.

We then compared the nanozyme activity of MSPLNP-Au in mimicked gastric conditions (SGF) and mimicked neutral intestinal conditions (simulated intestinal fluid (SIF)). MSPLNP-Au exhibited both oxidase- and peroxidase-like activity in the gastric condition (Figure 2d) but no oxidase/peroxidase-like activity under the intestinal condition (Figure 2e), indicating the pH-responsive activation of the MSPLNP-Au nanozyme. TMB generated an obvious yellow color quickly in the SGF in the presence of MSPLNP-Au, further showing that MSPLNP-Au still possessed the oxidase-like activity in gastric acid conditions (Figure 2f).

We further investigated the mechanism of the nanozyme activity of MSPLNP-Au. Various fluorescence probes were used to monitor the intermediates in the reaction system and to evaluate the ability of MSPLNP-Au to generate ROS. Hydroethidine is a selective fluorescence probe for the superoxide radical (O$_2^{•−}$) with an oxidization fluorescent product ethidium and corresponding fluorescence enhancement at 600−650 nm.[47] The fluorescence intensity of ethidium was obviously increased after adding MSPLNP-Au, indicating the excellent oxidase-like activity of MSPLNP-Au to generate O$_2^{•−}$ at acidic conditions (Figure S9). The peroxidase-like activity of MSPLNP-Au makes H$_2$O$_2$ decompose to generate a hydroxyl radical (●OH).[48] So, terephthalic acid was used to track the formation of ●OH because it could capture ●OH and generate 2-hydroxy terephthalic acid with unique fluorescence enhancement at 435 nm.[49] Figure S10 shows that the ●OH
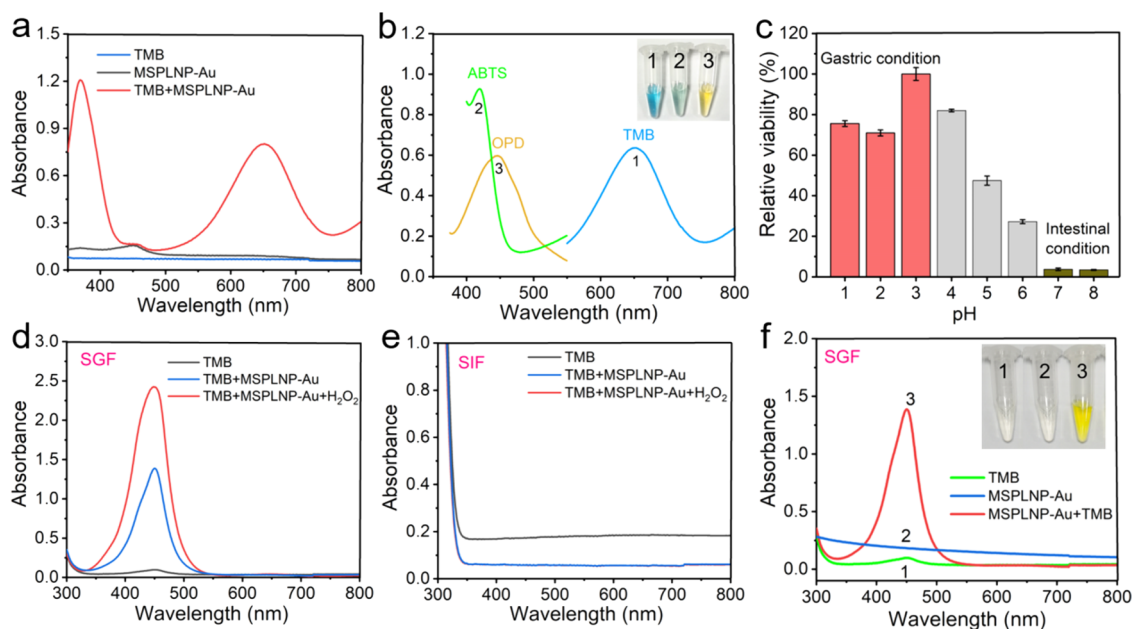
Figure 2. Characterization of the MSPLNP-Au nanozyme. (a) UV−vis spectra of TMB, MSPLNP-Au, and MSPLNP-Au+TMB in acetate buffer (pH 4.0, 30 min incubation). (b) MSPLNP-Au catalyzed oxidation of TMB (1), ABTS (2), and OPD (3) with the corresponding color changes. (c) pH-responsive oxidase-like activity of MSPLNP-Au. Data were calculated as means ± s.d. (n = 3). Oxidase- and peroxidase-like activity of the MSPLNP-Au in SGF (d) and SIF (e). (f) MSPLNP-Au catalyzed oxidation of TMB in the SGF.
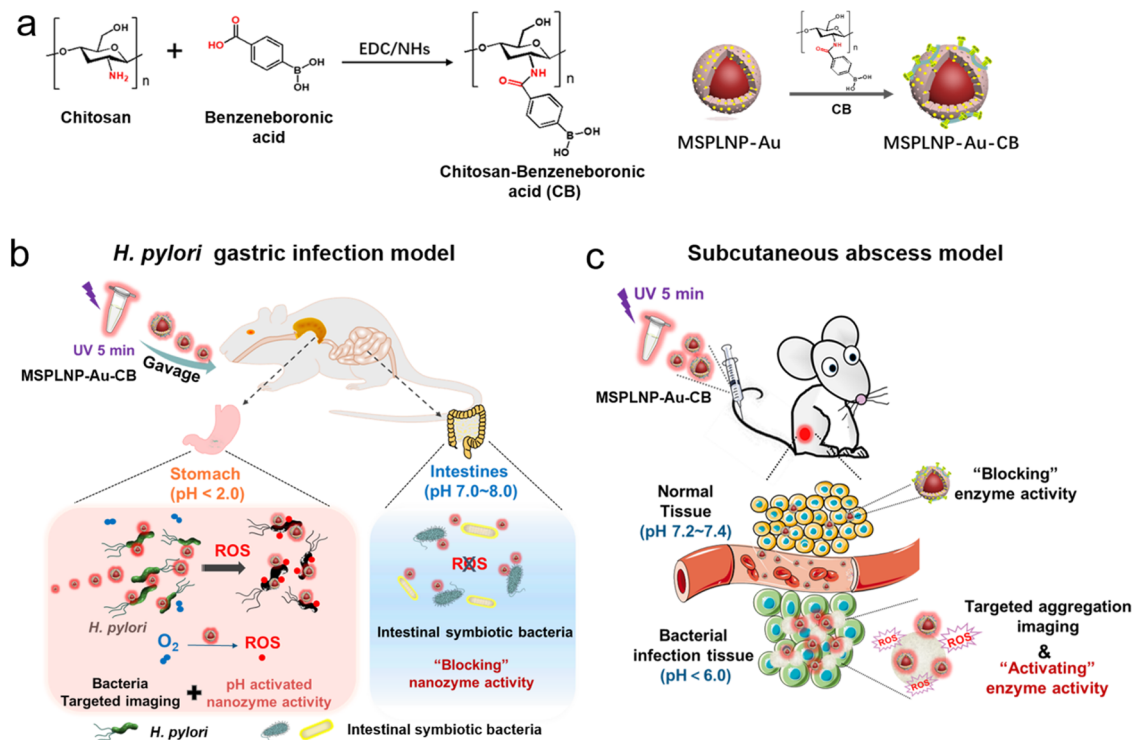

Figure 3. CB synthesis and MSPLNP-Au-CB targeted inactivation of bacteria. (a) Illustration of CB synthesis and MSPLNP-Au-CB functionalization. (b) Schematic of the MSPLNP-Au-CB nanozyme for targeted killing of *H. pylori* in the gastric environment without nonspecific damage to intestinal symbiotic bacteria in the intestinal environment. (c) Schematic for MRSA targeted inactivation based on the MSPLNP-Au-CB nanozyme.

was mainly generated from the decomposition of H_2O_2 catalyzed by MSPLNP-Au.

Chitosan-Benzeneboronic Acid (CB) Functionalization of MSPLNP-Au. The MSPLNP-Au exhibits excellent oxidase/peroxidase like activity for the generation of ROS. However, it is difficult for ROS, with high reactivity but a

limited diffusion distance, to act efficiently on bacteria, thus restricting their antibacterial activity and biosafety. Therefore, a combination of enzyme-like activity and a bacterial binding ability is the key to the increase in the concentration of ROS around the bacterial membrane and the reduction of the nonspecific side effects to normal cells. Boronic acid, a bacterial

binding molecule, can reversibly bind to peptidoglycans on the bacterial cell wall to realize the specific capture of target bacteria.[32] To achieve *H. pylori*-targeted adherence, we synthesized chitosan-benzeneboronic acid (CB) through the chemical bonding between the amine groups of chitosan and the carboxylic groups of 4-carboxyphenylboronic acid (Figure 3a). The synthesized CB was then characterized by ^{1}H NMR (Figure S11) and FT-IR (Figure S12). CB functionalization of MSPLNP-Au was achieved via electrostatic adsorption of the CB molecule on MSPLNP-Au and characterized by FT-IR spectra and the zeta potential (Figure S13). CB functionalization did not lead to the significant change of the PL property (Figure S14) and the nanozyme activity of MSPLNP-Au in the SGF (Figure S15). The prepared MSPLNP-Au-CB showed typical Michaelis−Menten kinetics and a pH-dependent enzyme-like property (Figure S16). In addition, MSPLNP-Au-CB also possessed an intrinsic oxidase-like activity even in a microaerobic atmosphere as indicated by the K_m and V_{max} values (Tables S1 and S2).

The obtained MSPLNP-Au-CB nanozyme possessed a red LED light-renewable long PL, pH-activated oxidase/peroxidase-like activity, and selective bacterial binding capability, being promising for selective imaging and killing of *H. pylori* and common resistant bacteria. In gastric acid conditions, MSPLNP-Au-CB would target *H. pylori*, and its nanozyme activity would be activated to catalyze ROS formation, getting targeted PL imaging and high local ROS concentration for effective *H. pylori* inactivation. However, the nanozyme activity of MSPLNP-Au-CB would be suppressed after entering the intestinal environment, avoiding nonspecific damage to intestinal commensal bacteria (Figure 3b). Meanwhile, because MSPLNP-Au-CB still maintained part of the effective nanozyme activity in slightly acidic conditions, its nanozyme activity would also be activated for targeted PL imaging and killing of bacteria in common bacterial infection acidic environments. Also, the nanozyme activity of MSPLNP-Au-CB would be suppressed under normal tissue conditions, avoiding nonspecific targeting of injury and allowing for its biocompatibility with normal tissues (Figure 3c).

pH-Responsive MSPLNP-Au-CB for Targeted PL Imaging and Killing of *H. pylori*. We then demonstrated the performance of MSPLNP-Au-CB targeted PL imaging and killing of *H. pylori*. The antibacterial capability of MSPLNP-Au-CB against *H. pylori* was first evaluated in vitro. MSPLNP-Au-CB exhibited efficient inhibition to the proliferation of *H. pylori* in a dose-dependent manner (Figure 4a). In addition, MSPLNP-Au-CB gave different bactericidal activities at pH 2.0 and pH 7.0: notable bacterial killing activity against *H. pylori* under acidic conditions (pH 2.0) but no bactericidal activity under normal tissue conditions (pH 7.0) (Figure 4b,c).

The performance of MSPLNP-Au-CB for targeting *H. pylori* was further demonstrated in vitro. Scanning electron microscopy (SEM) images show that *H. pylori* showed an intact cell wall and a typically spiral morphology before MSPLNP-Au-CB treatment but was completely ruptured with content leakage after incubation and surface attachment with MSPLNP-Au-CB (Figure 4d). The interaction between MSPLNP-Au-CB and *H. pylori* was observed on a laser confocal scanning microscope (LCSM). Incubation with MSPLNP-Au-CB led to a significant red luminescence on the bacteria from the inherent luminescence of the PLNP core (Figure 4e), indicating a superior bacterial targeting ability of MSPLNP-Au-CB.
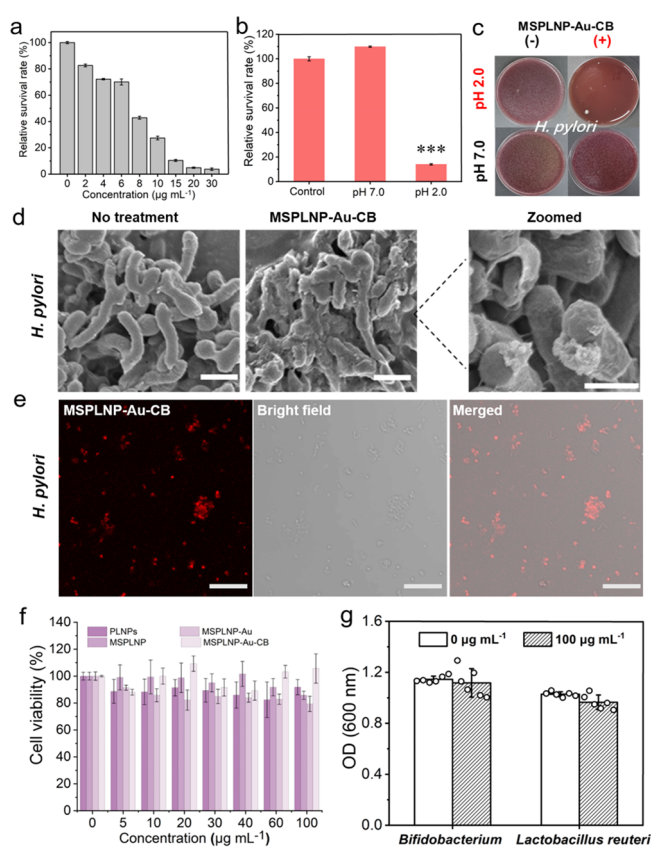

Figure 4. Performance of MSPLNP-Au-CB for targeted PL imaging and killing of *H. pylori*. (a) Relative *H. pylori* viability after incubating with different concentrations of MSPLNP-Au-CB. Data were calculated as means ± s.d. (n = 3). (b) Relative bactericidal activity of MSPLNP-Au-CB (30 μg mL^{-1}) under different conditions. Data were calculated as means ± s.d. (n = 3). P values were calculated by the Student's two-sided test (***p < 0.001). (c) Photos of *H. pylori* colonies under different conditions. (d) SEM images of *H. pylori* in the presence or absence of MSPLNP-Au-CB. Scale bar: 1.0 μm. (e) Representative LCSM images for *H. pylori* treated with MSPLNP-Au-CB. Scale bar: 10 μm. (f) Cytotoxicity assay of PLNP, MSPLNP, MSPLNP-Au, and MSPLNP-Au-CB. Data were calculated as means ± s.d. (n = 5). (g) Relative antibacterial activity of MSPLNP-Au-CB against intestinal symbiotic bacteria (MSPLNP-Au-CB, 100 μg mL^{-1}). Data were calculated as means ± s.d. (n = 6).

The cytotoxicity of MSPLNP-Au-CB was primarily evaluated via MTT assay. MSPLNP-Au-CB exhibited negligible inhibition to the proliferation of 3T3 cells, with the cell viability remaining over 85% even at over threefold of the effective bactericidal concentration (100 μg mL^{-1}) (Figure 4f). On the other hand, *Bifidobacterium* and *Lactobacillus reuteri*, two of the important intestinal symbiotic bacteria, were used to evaluate the harmful effect of MSPLNP-Au-CB on the intestinal environment. Compared with the control group, MSPLNP-Au-CB gave no antibacterial activity against *Bifidobacterium* and *Lactobacillus reuteri*, showing that MSPLNP-Au-CB exhibited no nanozyme activity under intestinal conditions and no obvious side effects on intestinal symbiotic bacteria (Figure 4g and Figure S17). All these results indicate the effective pH-responsive bacterial inactivation of the MSPLNP-Au-CB nanozyme toward bacteria under bacterial infection acidic conditions but superior biocompatibility toward intestinal symbiotic bacteria and normal cells under normal physiological conditions.

The performance of MSPLNP-Au-CB for in vivo targeting, imaging and, inactivation of *H. pylori* was then investigated with an *H. pylori*-infected mouse model. Each mouse received gavage with *H. pylori* (10^9 CFU mL^{-1}) once daily for consecutive 4 days (Figure 5a). After 1 week of infection,
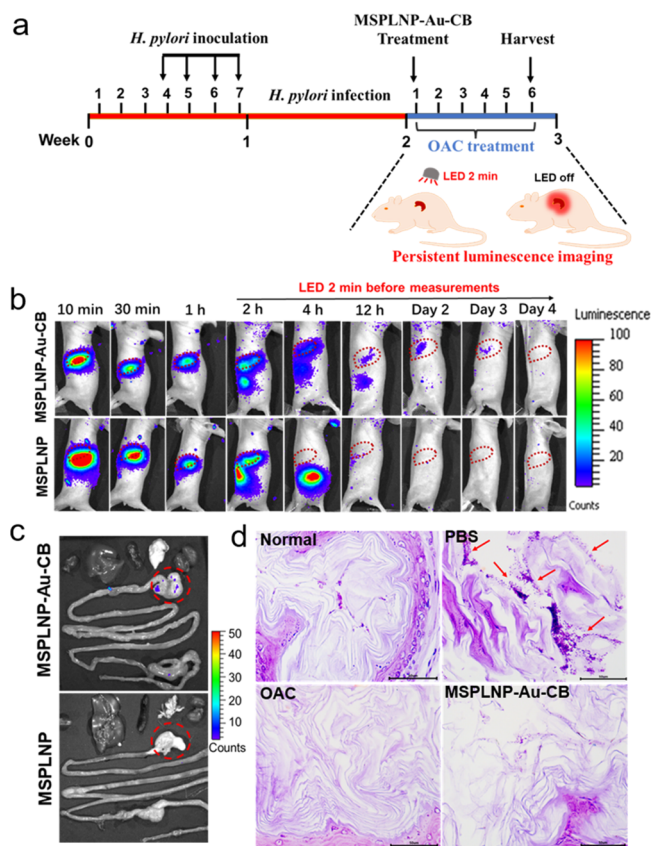

Figure 5. Performance of MSPLNP-Au-CB for in vivo targeting, imaging, and inactivation of *H. pylori*. (a) Schedule for PL imaging and treatment in mice, including *H. pylori* inoculation, infection development, and therapy before harvest. (b) Time-dependent PL images of the *H. pylori*-infected mouse model after MSPLNP-Au-CB gavage. (c) Ex vivo PL images of major organs excised from mice on day 6 after MSPLNP-Au-CB gavage. (d) Gram staining of the gastric mucosa slice from the mice in PBS, MSPLNP-Au-CB, OAC, and normal groups. Red arrows point to *H. pylori*. The scale bar is 50 μm.

bacterial burden in the mouse stomach was quantified to be 2.0 × 10^6 CFU per gram of the stomach tissue (Figure S18). Furthermore, the observation of *H. pylori* in the infected mouse gastric mucosa slice by Gram staining also demonstrated the successful establishment of the *H. pylori*-infected mouse model (Figure S19). Then, PL imaging of MSPLNP-Au-CB was visualized to monitor the retention of MSPLNP-Au-CB in the stomach of the mouse model (Figure 5b). Compared with the MSPLNP group, the luminescence imaging of the MSPLNP-Au-CB group in the mouse stomach was gradually clear at 4 h after oral gavage and continued until day 3, realizing a long retention time compared with the normal gastric emptying time of mice.[50] To further confirm the retention of MSPLNP-Au-CB in the stomach of the mouse model, the mouse stomach was excised at day 6 after intragastric administration. The luminescence signal in the excised stomach also indicates the effective retention of MSPLNP-Au-CB in the stomach (Figure 5c.).

H. pylori-infected mouse models were randomly divided into three treatment groups (the PBS group, MSPLNP-Au-CB therapy group, and antibiotic triple therapy OAC group) as well as a blank control group of healthy mice. The mice in the MSPLNP-Au-CB group received only one time gavage of MSPLNP-Au-CB. The mice in the OAC group received antibiotics once daily for 6 consecutive days (first received omeprazole 30 min before amoxicillin and clarithromycin oral gavage). The Gram staining images of gastric tissues in the MSPLNP-Au-CB group show no obvious bacterial presence after the 6 day treatment, similar to those in the OAC group and the blank control group (Figure 5d). However, a collection of bacteria still existed in the gastric tissue of mice in the PBS group, indicating that the MSPLNP-Au-CB nanozyme was activated in the stomach and exhibited effective *H. pylori* killing in vivo.

We further explored the harmful effect of MSPLNP-Au-CB during in vivo treatment. No obvious changes in the body weight of mice were observed during MSPLNP-Au-CB treatment (Figure S20), indicating the low toxicity of MSPLNP-Au-CB. The hematoxylin−eosin (H&E) staining images of gastric tissues of mice in the MSPLNP-Au-CB group show no obvious damage and inflammation with a clear arrangement of epithelial cells, similar to the gastric sample of normal mice (Figure S21). In addition, almost no luminescence of MSPLNP-Au-CB was observed in other visceral organs except the stomach, demonstrating superior biocompatibility of intragastric administration with MSPLNP-Au-CB (Figure 5c and Figure S22). Most importantly, the side effect of MSPLNP-Au-CB on the intestinal symbiotic microbe was also evaluated. The intestinal microbial richness level of mice in the MSPLNP-Au-CB group was consistent with the mice in the normal group, while the antibiotic therapy OAC group significantly reduced the richness level due to the undesired side effect of antibiotics (Figure 6a). The beta diversity analysis of the intestinal microflora further demonstrated similar microbial community composition of the mice treated with MSPLNP-Au-CB and the normal mice but a significant difference from the mice treated with the OAC antibiotic (Figure 6b). In addition, the heatmap analysis of the intestinal contents showed similar species abundance of samples in the MSPLNP-Au-CB group and the normal group on a genus level but obviously different species abundance in the OAC group with the level downward revision of most of the bacterial genera (Figure 6c). The results indicate that the pH-responsive PL nanozyme could only be activated in the gastric acid microenvironment for selective targeting and inactivation of *H. pylori* in vivo without damage toward normal tissues and intestinal symbiotic bacteria.

pH-Responsive MSPLNP-Au-CB for Targeted PL Imaging and Killing of *E. coli*, *S. aureus*, and MRSA. Since MSPLNP-Au-CB still maintains effective nanozyme activity in a slightly acidic environment, it should also keep the capability to kill *Escherichia coli* (*E. coli*), *Staphylococcus aureus* (*S. aureus*), and methicillin-resistant *Staphylococcus aureus* (MRSA) under common acidic conditions of bacterial infection (PBS, pH 5.5). MSPLNP-Au-CB at no more than 50 μg mL^{-1} suppressed more than 99% of the studied three bacterial strains at pH 5.5 (30 μg mL^{-1} MSPLNP-Au-CB suppressed 99.2% *E. coli*, 96.5% *S. aureus*, and 98.4% MRSA) (Figure 7a−e). However, MSPLNP-Au-CB gave no significant antibacterial capability in a normal physiological environment (pH 7.0) (Figure 7d,e). The interaction between MSPLNP-
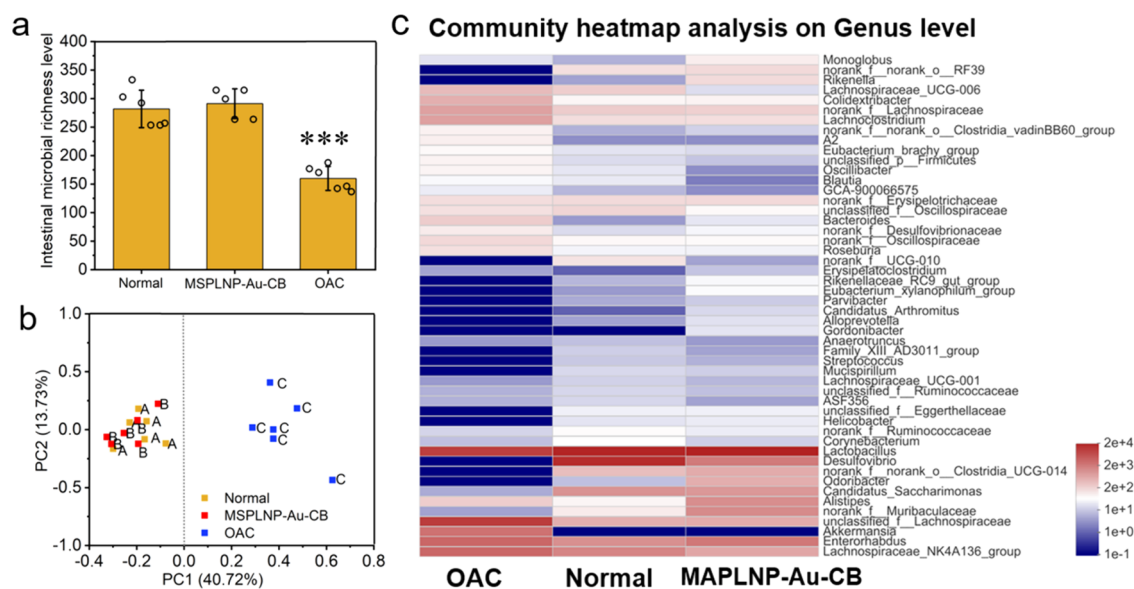
Figure 6. Characterization of the harmful effect of MSPLNP-Au-CB to the intestinal symbiotic microbe. (a) Alpha diversity analysis for the intestinal microbial richness. Data were calculated as means ± s.d. ($n = 5$). *P* values were calculated by the Student's two-sided test (***$p < 0.001$). (b) Beta diversity analysis for the intestinal microflora by principal coordinates analysis. (c) Community heatmap analysis on the genus level of the intestinal contents in different treatment groups.

Au-CB and the studied three bacterial strains was observed on an LCSM. MSPLNP-Au-CB led to significant red luminescence on the bacteria, indicating an excellent targeting ability of MSPLNP-Au-CB to the bacterial strains (Figure 7f). Moreover, the morphology of the bacterial strains was directly visualized by SEM before and after treating with MSPLNP-Au-CB. Bacterial strains showed an integrated and smooth surface before incubating with MSPLNP-Au-CB. However, MSPLNP-Au-CB treatment led to significant damage of the bacteria cells of *E. coli*, *S. aureus*, and MRSA with the wrinkled and ruptured cell wall (Figure 7g). These results show the capability of MSPLNP-Au-CB for pH-responsive and targeted bacterial killing in common acidic environments of bacterial infection.

In view of the excellent antibacterial capability of MSPLNP-Au-CB against *E. coli*, *S. aureus*, and MRSA in vitro, an MRSA-infected subcutaneous abscess mouse model was established to further evaluate the performance of MSPLNP-Au-CB for in vivo targeting, imaging, and therapy (Figure S23). The treatment schedule of MSPLNP-Au-CB is illustrated in Figure 8a. The subcutaneous abscess mouse model was intravenously injected with MSPLNP and MSPLNP-Au-CB. Figure 8b shows time-dependent luminescence accumulation in the abscess site of the mice in the MSPLNP-Au-CB group. The luminescence signal in the abscess area appeared at 1 h after injection, gradually became significant, and reached the maximum at day 2. Afterward, the luminescence signal gradually diminished and completely disappeared at day 6. In contrast, the luminescence signal was hard to see in the abscess region of the mice in the MSPLNP group at all time points. These results show that MSPLNP-Au-CB had good in vivo targeted PL imaging of MRSA infection.

The MRSA-infected mice were randomly divided into three treatment groups (the PBS group, MSPLNP group, and MSPLNP-Au-CB group) with normal mice as a blank control group for comparison. Mice in the three treatment groups were intravenously injected with PBS, MSPLNP, and MSPLNP-Au-CB. The abscess and inflammation on the skin in the MSPLNP-Au-CB group disappeared at day 8 but still remained on the skin of the mice in the MSPLNP group and the PBS group (Figure 8c). The quantitative bacterial colonies were significantly reduced in the MSPLNP-Au-CB group after the 10 day treatment, indicating great recovery from infection (Figure 8d). H&E staining shows obvious scab and massive inflammatory cell infiltration in the abscess skin of the mice in the MSPLNP group and the PBS group (Figure 8e). Like the blank control group, the skin of the mice in the MSPLNP-Au-CB group showed less severe inflammatory cell infiltration and more reconstructed hair follicles. Moreover, the MSPLNP-Au-CB group gave a dramatically lower level of the blood inflammatory factor IL-6 and IL-1β than the other two groups but a similar level to the mice in the blank control group (Figure 8f,g), confirming the good therapeutic effect on the infected mice in the MSPLNP-Au-CB group.

The mouse model exhibited no obvious changes in the body weight during the MSPLNP-Au-CB 10 day treatment, indicating low toxicity of the MSPLNP-Au-CB nanozyme (Figure S24). The relative PL intensity of isolated organs showed the highest MSPLNP-Au-CB in the liver and the spleen because of the strong phagocytosis of the reticuloendothelial system but was negligible in other organs (Figure S25). All these results demonstrate that the MSPLNP-Au-CB nanozyme can be effectively activated in the MRSA bacterial infection abscesses with multiple drug resistance bacterial killing capability in vivo.

CONCLUSIONS

We have developed a stable pH-responsive persistent luminescence nanozyme (MSPLNP-Au-CB) for targeted killing of *H. pylori*. The developed nanozyme gets the merit of pH-responsive, oxidase- and peroxidase-like dual nanozyme activity to produce bactericidal ROS. With the integration of red LED light-renewable long persistent luminescence of PLNP and selective bacterial targeting capability of CB, this nanozyme allows for targeted luminescence imaging and effective bacterial inactivation toward *H. pylori* in extreme gastric acid environments and MRSA in common slightly
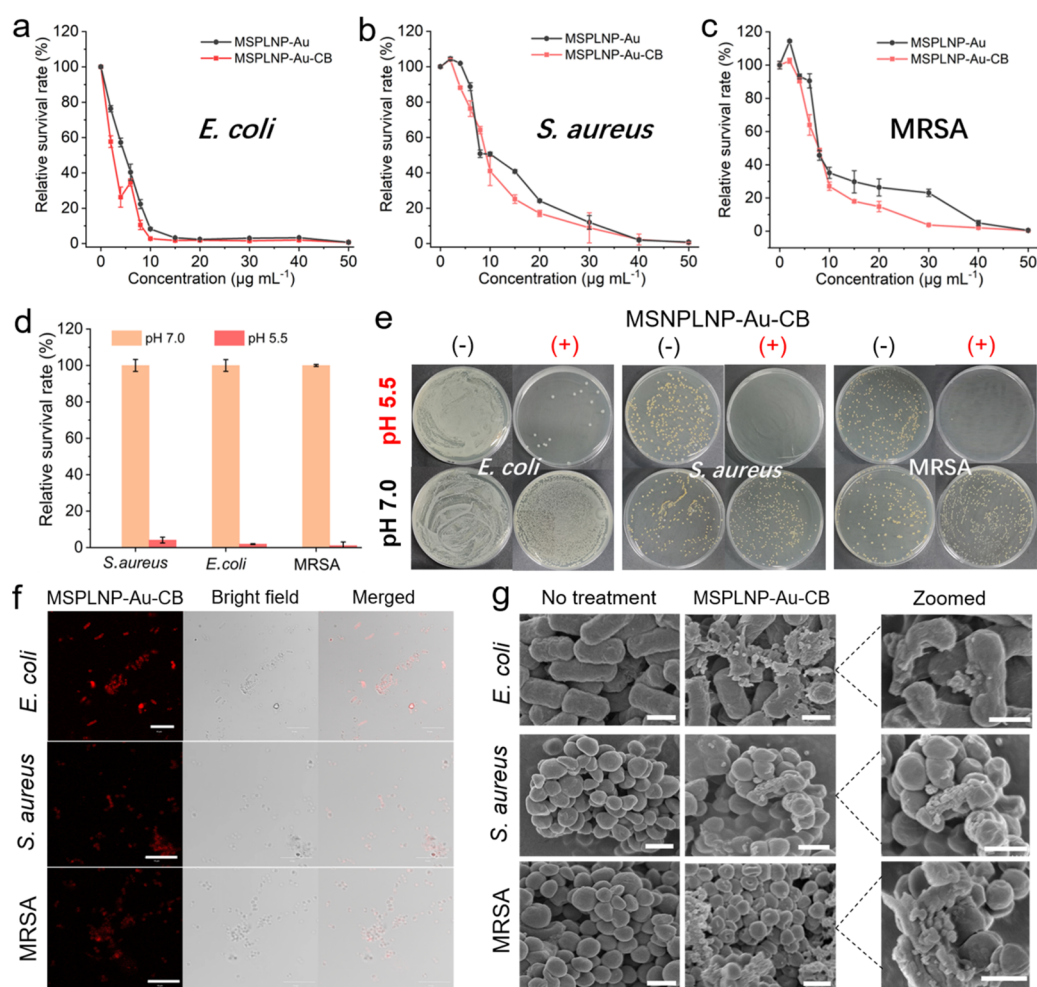
Figure 7. Performance of MSPLNP-Au-CB for targeted PL imaging and killing of *E. coli*, *S. aureus*, and MRSA. Relative viability for *E. coli* (a), *S. aureus* (b), and MRSA (c) after incubating with MSPLNP-Au and MSPLNP-Au-CB. Data were calculated as means ± s.d. (n = 3). (d) Relative bactericidal activity of MSPLNP-Au-CB (30 μg mL^{-1}) against bacteria under an acidic environment (pH 5.5) and a normal physiological environment (pH 7.0). Data were calculated as means ± s.d. (n = 3). (e) Photos of *E. coli*, *S. aureus*, and MRSA colonies treated with MSPLNP-Au-CB (30 μg mL^{-1}) at different pH values. (f) Representative LCSM images of *E. coli*, *S. aureus*, and MRSA treated with MSPLNP-Au-CB (30 μg mL^{-1}). Scale bar: 10 μm. (g) SEM images of *E. coli*, *S. aureus*, and MRSA before and after MSPLNP-Au-CB treatment. Scale bar: 1.0 μm.

acidic environments but has a negligible harmful effect on intestinal symbiotic bacteria and normal tissues. Such a pH-activatable nanozyme contains no antibiotics and shows promise to overcome the critical challenges in selective therapy of drug-resistant bacterial infection even at specific environments.

■ EXPERIMENTAL SECTION

Synthesis of MSPLNP. The used PLNP $Zn_{1.2}Ga_{1.6}Ge_{0.2}O_4$:$Cr^{3+}$ was synthesized according to our previous work.[43,51] TEA (68 mg) was dissolved in deoxygenated water (25 mL) at 80 °C. Then, PLNP (80 mg), NaSal (42 mg), and CTAB (380 mg) were added to the solution of TEA. The mixture was stirred for 1 h, and TEOS (500 μL) was added. Thirty, 60, 90, and 120 min later, APTES was added to the solution four times (20 μL each time). The mixture was kept stirring for 2 h. The product was collected by centrifugation and washed three times with ethanol. Subsequently, CTAB was extracted with ethanol (50 mL of ethanol containing 3 mL of 37% HCl) for 6 h (three times) at 70 °C. The resulting MSPLNP was washed with ethanol and water and collected by centrifugation and dried under vacuum.

Preparation of MSPLNP-Au. MSPLNP (5 mg) were dispersed in distilled water (2 mL) under sonication for 10 min followed by the addition of HAuCl$_4$ solution (40 μL, 20 mmol L^{-1}). After 1 h of stirring, freshly prepared NaBH$_4$ (10 μL, 60 mmol L^{-1}) was added

into the above solution, and the resulting suspension was stirred for another 1 h. The resulting MSPLNP-Au was washed with water, collected by centrifugation, and dried under vacuum.

Oxidase- and Peroxidase-like Property of MSPLNP-Au. Certain amounts of MSPLNP-Au and TMB (4 μL, final concentration of 800 μmol L^{-1}) were added into acetate buffer solution (200 μL, 25 mmol L^{-1}, pH 4.0). The mixture solution was reacted at 37 °C for 30 min and centrifuged to get the supernatant for the measurement of UV−vis absorption spectra. TMB was replaced by other organic dyes ABTS and OPD to further confirm the oxidase-like property of MSPLNP-Au in the same way. The peroxidase-like property of MSPLNP-Au was evaluated in the same way with the addition of 12.5 μL of H$_2$O$_2$ (final concentration of 50 mmol L^{-1}). Data were calculated as means ± s.d. (n = 3).

The same method was applied to evaluate the oxidase- and peroxidase-like property of MSPLNP-Au in the SGF and the SIF by replacing acetate buffer solution with SGF or SIF solution (200 μL).

Luminescence Imaging of MSPLNP-Au-CB in an *H. pylori*-Infected Mouse Model. The *H. pylori*-infected mice were administrated with MSPLNP (100 μL, 2 mg mL^{-1}) and MSPLNP-Au-CB (100 μL, 2 mg mL^{-1}) by oral gavage. Then, the luminescence distribution of MSPLNP-Au-CB in the mouse stomach was monitored at designated time points. The distribution of the luminescence of MSPLNP was monitored for comparison.
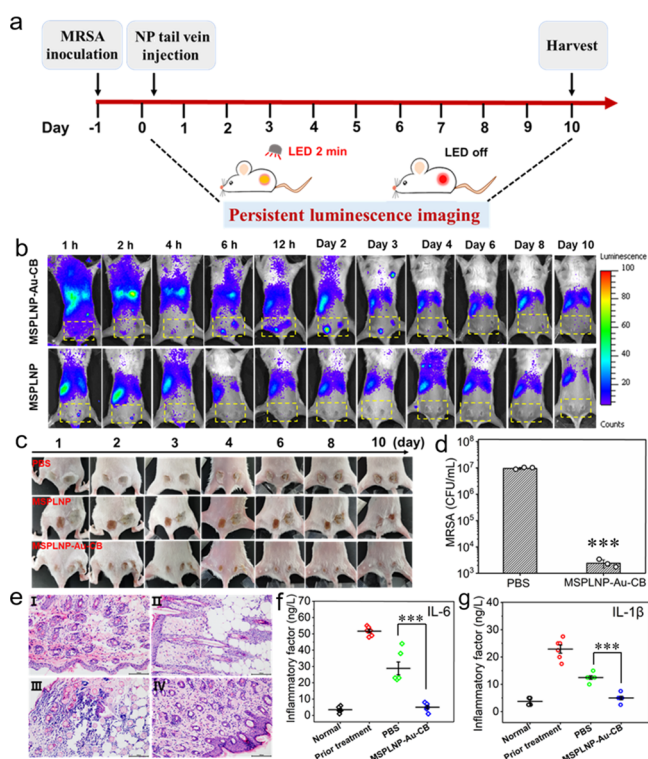
Figure 8. Performance of MSPLNP-Au-CB for in vivo targeting, imaging, and inactivation of MRSA. (a) Treatment schedule for PL imaging and therapy in a mouse model, including MRSA inoculation, infection development, and therapy before harvest. (b) Time-dependent PL images after intravenous injection with MSPLNP-Au-CB into a mouse model. (c) Representative photos of the infection part of a mouse model with various treatments for 10 days. (d) Corresponding results of bacterial cultures for the tissues of MRSA-infected mice in different therapy groups. Data were calculated as means ± s.d. ($n = 3$). (e) Histological staining of the skin slice from the abscess sites of the mice in different therapy groups (I–IV represent the MSPLNP-Au-CB group, PBS group, MSPLNP group, and blank control group, respectively) (scale bar, 100 μm). IL-6 level (f) and IL-1β level (g) in blood of mice with 10 day different treatments. Data were calculated as means ± s.d. ($n = 6$). P values were calculated by the Student's two-sided test (*** $p < 0.001$).

Luminescence Imaging of MSPLNP-Au-CB in an MRSA-Infected Subcutaneous Abscess Mouse Model. MSPLNP and MSPLNP-Au-CB (100 μL, 2 mg mL^{-1}) were intravenously injected into anesthetized MRSA-infected mice. The luminescence of MSPLNP-Au-CB was monitored at designated time points. The distribution of the luminescence of MSPLNP was monitored for comparison.

MSPLNP-Au-CB Targeted Treatment for *H. pylori* Infection In Vivo. The established *H. pylori*-infected mice ($n = 15$) were randomly divided into three treatment groups (five mice for each group) to receive PBS, MSPLNP-Au-CB, or triple therapy OAC (omeprazole, amoxicillin, and clarithromycin) by oral administration. The performance of triple therapy was evaluated according to Zhang et al.[32] The triple therapy group received antibiotics once daily for 6 consecutive days. The MSPLNP-Au-CB group received only one gavage of MSPLNP-Au-CB (100 μL, 2 mg mL^{-1}). The group of mice treated with PBS was used as a negative control. After the 6 day treatment, the three groups of mice were sacrificed, and the stomachs were excised from the abdominal cavity for bacterial colonization and tissue section staining. The intestines of the mice were also collected to reveal the effect of MSPLNP-Au-CB on the symbiotic bacteria. The intestine symbiotic bacteria were determined by a quantitative real-

time PCR method.[52,53] The primer sequences for quantitative real-time PCR are listed in Table S3.

MSPLNP-Au-CB for Selective In Vivo Treatment of an MRSA-Infected Subcutaneous Abscess Mouse Model. After 24 h of MRSA infection, the mice ($n = 15$) were randomly divided into three groups (five mice for each group): the PBS group, MSPLNP group, and MSPLNP-Au-CB group. Normal mice were used as a blank control group for comparison. The mice in the PBS group and the MSPLNP-Au-CB group were intravenously injected with PBS (100 μL) and MSPLNP-Au-CB (100 μL, 2 mg mL^{-1}), respectively. All mice were sacrificed after the 10 day treatment, and IL-6 and IL-1β in the serum of mouse blood in the four groups studied were determined according to our previous work.[43] The skin tissues and major organs were fixed in a 4% formaldehyde solution for H&E staining.

■ ASSOCIATED CONTENT

Ⓢ Supporting Information

The Supporting Information is available free of charge at https://pubs.acs.org/doi/10.1021/acsami.1c21318.

> Additional information including supplementary materials, characterization, methods, supplementary figures of the morphology, structure, and luminescence properties of the prepared PLNP and MSPLNP, stability of MSPLNP-Au, nanozyme activity of the MSPLNP-Au and MSPLNP-Au-CB, ^{1}H NMR spectra of CB, FT-IR spectra of CB and MSPLNP-Au-CB, photos of *Bifidobacterium* and *Lactobacillus reuteri* colonies, photograph and quantification of *H. pylori* colonies, tissue section staining and H&E staining of a gastric mucosa slice of the mouse model, body weight changes of the mouse model, ex vivo persistent luminescence intensity of major organs, skin tissue section staining of the mouse model, and supplementary tables of the Michaelis–Menten constant (K_m) and maximal reaction velocity (V_{max}) for the oxidase-like and peroxidase-like activity of MSPLNP-Au-CB and sequences of the primers for PCR (PDF)

■ AUTHOR INFORMATION

Corresponding Author

Xiu-Ping Yan − *State Key Laboratory of Food Science and Technology, International Joint Laboratory on Food Safety, Institute of Analytical Food Safety, School of Food Science and Technology, and Key Laboratory of Synthetic and Biological Colloids, Ministry of Education, Jiangnan University, Wuxi 214122, China;* ⓞ orcid.org/0000-0001-9953-7681; Email: xpyan@jiangnan.edu.cn

Authors

Li-Xia Yan − *State Key Laboratory of Food Science and Technology, International Joint Laboratory on Food Safety, and Institute of Analytical Food Safety, School of Food Science and Technology, Jiangnan University, Wuxi 214122, China*

Bei-Bei Wang − *State Key Laboratory of Food Science and Technology, International Joint Laboratory on Food Safety, and Institute of Analytical Food Safety, School of Food Science and Technology, Jiangnan University, Wuxi 214122, China;* ⓞ orcid.org/0000-0002-6139-9495

Xu Zhao − *State Key Laboratory of Food Science and Technology, International Joint Laboratory on Food Safety, and Institute of Analytical Food Safety, School of Food*

Science and Technology, Jiangnan University, Wuxi 214122, China; ⓘ orcid.org/0000-0001-8000-9045

Li-Jian Chen − *State Key Laboratory of Food Science and Technology, International Joint Laboratory on Food Safety, and Institute of Analytical Food Safety, School of Food Science and Technology, Jiangnan University, Wuxi 214122, China;* ⓘ orcid.org/0000-0001-8671-8766

Complete contact information is available at:
https://pubs.acs.org/10.1021/acsami.1c21318

Notes

The authors declare no competing financial interest.

■ REFERENCES

(1) Sasaki, T.; Saito, R.; Oyama, M.; Takeuchi, T.; Tanaka, T.; Natsume, H.; Tamura, M.; Arata, Y.; Hatanaka, T. Galectin-2 Has Bactericidal Effects against *Helicobacter pylori* in a β-Galactoside-Dependent Manner. *Int. J. Mol. Sci.* **2020**, *21*, 2697.

(2) Kouitcheu, L. B.; Mabeku, M. L.; Ngamga, N.; Leundji, H. Potential Risk Factors and Prevalence of *Helicobacter pylori* Infection among Adult Patients with Dyspepsia Symptoms in Cameroon. *BMC Infect. Dis.* **2018**, *18*, 278.

(3) Buzás, G. M. Benign and Malignant Gastroduodenal Diseases Associated with *Helicobacter pylori*: A Narrative Review and Personal Remarks in 2018. *Minerva Gastroenterol Dietol.* **2018**, *64*, 280−296.

(4) Marques, V.; Cunha, B.; Couto, A.; Sampaio, P.; Fonseca, L. P.; Aleixo, S.; Calado, C. R. C. Characterization of Gastric Cells Infection by Diverse *Helicobacter pylori* Strains through Fourier-Transform Infrared Spectroscopy. *Spectrochim. Acta A Mol. Biomol. Spectrosc.* **2019**, *210*, 193−202.

(5) Tonkic, A.; Tonkic, M.; Lehours, P.; Mégraud, F. Epidemiology and Diagnosis of *Helicobacter pylori* Infection. *Helicobacter* **2012**, *17*, 1−8.

(6) Zhang, Y.; Sun, H.; Chen, X.; Li, J.; Zhao, H.; Geng, L.; Li, B. Functional Profile of Gastric Epithelial Cells Infected with *Helicobacter pylori* Strains. *Microbial pathogenesis.* **2016**, *95*, 77−81.

(7) Zhang, X.-Y.; Zhang, P.-Y.; Aboul-Soud, M. A. M. From Inflammation to Gastric Cancer: Role of *Helicobacter pylori*. *Oncol. Lett.* **2017**, *13*, 543−548.

(8) Sugano, K.; Kuipers, E. J.; Graham, D. Y.; El-Omar, E. M.; Miura, S.; Haruma, K.; Asaka, M.; Uemura, N.; Malfertheiner, P. Kyoto Global Consensus Report on *Helicobacter pylori* Gastritis. *Gut* **2015**, *64*, 1353−1367.

(9) Flores-Treviño, S.; Mendoza-Olazarán, S.; Bocanegra-Ibarias, P.; Maldonado-Garza, H. J.; Garza-González, E. *Helicobacter pylori* Drug Resistance: Therapy Changes and Challenges. *Expert Rev. Gastroenterol. Hapatol.* **2018**, *12*, 819−827.

(10) Xiong, M.; Bao, Y.; Xu, X.; Wang, H.; Han, Z.; Wang, Z.; Liu, Y.; Huang, S.; Song, Z.; Chen, J.; Peek, R. M., Jr.; Yin, L.; Chen, L.-F.; Cheng, J. Selective Killing of *Helicobacter pylori* with pH-Responsive Helix-Coil Conformation Transitionable Antimicrobial Polypeptides. *Proc. Natl. Acad. Sci. U. S. A.* **2017**, *114*, 12675−12680.

(11) Mégraud, F. Current Recommendations for *Helicobacter pylori* Therapies in a World of Evolving Resistance. *Gut Microbes* **2013**, *4*, 541−548.

(12) Mégraud, F. *Helicobacter pylori* and Antibiotic Resistance. *Gut* **2007**, *56*, 1502.

(13) Tacconelli, E.; Carrara, E.; Savoldi, A.; Harbarth, S.; Mendelson, M.; Monnet, D. L.; Pulcini, C.; Kahlmeter, G.; Kluytmans, J.; Carmeli, Y.; Ouellette, M.; Outterson, K.; Patel, J.; Cavaleri, M.; Cox, E. M.; Houchens, C. R.; Grayson, M. L.; Hansen, P.; Singh, N.; Theuretzbacher, U.; Magrini, N.; Aboderin, A. O.; al-Abri, S. S.; Awang Jalil, N.; Benzonana, N.; Bhattacharya, S.; Brink, A. J.; Burkert, F. R.; Cars, O.; Cornaglia, G.; Dyar, O. J.; Friedrich, A. W.; Gales, A. C.; Gandra, S.; Giske, C. G.; Goff, D. A.; Goossens, H.; Gottlieb, T.; Guzman Blanco, M.; Hryniewicz, W.; Kattula, D.; Jinks, T.; Kanj, S. S.; Kerr, L.; Kieny, M. P.; Kim, Y. S.; Kozlov, R. S.; Labarca, J.; Laxminarayan, R.; Leder, K.; Leibovici, L.; Levy-Hara, G.; Littman, J.; Malhotra-Kumar, S.; Manchanda, V.; Moja, L.; Ndoye, B.; Pan, A.; Paterson, D. L.; Paul, M.; Qiu, H.; Ramon-Pardo, P.; Rodríguez-Baño, J.; Sanguinetti, M.; Sengupta, S.; Sharland, M.; Si-Mehand, M.; Silver, L. L.; Song, W.; Steinbakk, M.; Thomsen, J.; Thwaites, G. E.; van der Meer, J. W. M.; van Kinh, N.; Vega, S.; Villegas, M. V.; Wechsler-Fördös, A.; Wertheim, H. F. L.; Wesangula, E.; Woodford, N.; Yilmaz, F. O.; Zorzet, A. Discovery, Research and Development of New Antibiotics: The WHO Priority List of Antibiotic-Resistant Bacteria and Tuberculosis. *Lancet Infect. Dis.* **2018**, *18*, 318−327.

(14) Tao, Y.; Ju, E.; Ren, J.; Qu, X. Bifunctionalized Mesoporous Silica-Supported Gold Nanoparticles: Intrinsic Oxidase and Peroxidase Catalytic Activities for Antibacterial Applications. *Adv. Mater.* **2015**, *27*, 1097−1104.

(15) Fang, G.; Li, W.; Shen, X.; Perez-Aguilar, J. M.; Chong, Y.; Gao, X.; Chai, Z.; Chen, C.; Ge, C.; Zhou, R. Differential Pd-Nanocrystal Facets Demonstrate Distinct Antibacterial Activity against Gram-Positive and Gram-Negative Bacteria. *Nat. Commun.* **2018**, *9*, 129.

(16) Cai, S.; Jia, X.; Han, Q.; Yan, X.; Yang, R.; Wang, C. Porous Pt/Ag Nanoparticles with Excellent Multifunctional Enzyme Mimic Activities and Antibacterial Effects. *Nano Res.* **2017**, *10*, 2056−2069.

(17) Xu, B.; Wang, H.; Wang, W.; Gao, L.; Li, S.; Pan, X.; Wang, H.; Yang, H.; Meng, X.; Wu, Q.; Zheng, L.; Chen, S.; Shi, X.; Fan, K.; Yan, X.; Liu, H. A Single Atom Nanozyme for Wound Disinfection Applications. *Angew. Chem., Int. Ed.* **2019**, *58*, 4911−4916.

(18) Kong, F.; Bai, H.; Ma, M.; Wang, C.; Xu, H.; Gu, N.; Zhang, Y. Fe$_3$O$_4$@Pt Nanozymes Combining with CXCR4 Antagonists to Synergistically Treat Acute Myeloid Leukemia. *Nano Today* **2021**, *37*, 101106.

(19) Zeng, L.; Cheng, H.; Dai, Y.; Su, Z.; Wang, C.; Lei, L.; Lin, D.; Li, X.; Chen, H.; Fan, K.; Shi, S. In vivo Regenerable Cerium Oxide Nanozyme-Loaded pH/H$_2$O$_2$-Responsive Nanovesicle for Tumor-Targeted Photothermal and Photodynamic Therapies. *ACS Appl. Mater. Interfaces* **2021**, *13*, 6451−6461.

(20) Herget, K.; Hubach, P.; Pusch, S.; Deglmann, P.; Götz, H.; Gorelik, T. E.; Gural'skiy, I.'y. A.; Pfitzner, F.; Link, T.; Schenk, S.; Panthöfer, M.; Ksenofontov, V.; Kolb, U.; Opatz, T.; André, R.; Tremel, W. Haloperoxidase Mimicry by CeO$_{2-X}$ Nanorods Combats Biofouling. *Adv. Mater.* **2017**, *29*, 1603823.

(21) Yin, W.; Yu, J.; Lv, F.; Yan, L.; Zheng, L. R.; Gu, Z.; Zhao, Y. Functionalized Nano-MoS$_2$ with Peroxidase Catalytic and Near-infrared Photothermal Activities for Safe and Synergetic Wound Antibacterial Applications. *ACS Nano* **2016**, *10*, 11000−11011.

(22) Cao, F.; Zhang, L.; Wang, H.; You, Y.; Wang, Y.; Gao, N.; Ren, J.; Qu, X. Defect-Rich Adhesive Nanozymes as Efficient Antibiotics for Enhanced Bacterial Inhibition. *Angew. Chem., Int. Ed.* **2019**, *58*, 16236−16242.

(23) Li, W.; Liu, C.; Guan, Y.; Ren, J.; Qu, X. Manganese Dioxide Nanozymes as Responsive Cytoprotective Shells for Individual Living Cell Encapsulation. *Angew. Chem., Int. Ed.* **2017**, *56*, 13661−113665.

(24) Wang, H.; Fu, W.; Chen, Y.; Xue, F.; Shan, G. ZIF-67-Derived Co$_3$O$_4$ Hollow Nanocage with Efficient Peroxidase Mimicking

Characteristic for Sensitive Colorimetric Biosensing of Dopamine. *Spectrochim. Acta, Part A* **2021**, *246*, 119006.

(25) Ding, S.; He, L.; Bian, X.; Tian, G. Metal-Organic Frameworks-Based Nanozymes for Combined Cancer Therapy. *Nano Today* **2020**, *35*, 100920.

(26) Ling, P.; Cheng, S.; Chen, N.; Qian, C.; Gao, F. Nanozyme-Modified Metal-Organic Frameworks with Multienzymes Activity as Biomimetic Catalysts and Electrocatalytic Interfaces. *ACS Appl. Mater. Interfaces* **2020**, *12*, 17185−17192.

(27) Wang, Y.; Zhao, M.; Ping, J.; Chen, B.; Cao, X.; Huang, Y.; Tan, C.; Ma, Q.; Wu, S.; Yu, Y.; Lu, Q.; Chen, J.; Zhao, W.; Ying, Y.; Zhang, H. Bioinspired Design of Ultrathin 2D Bimetallic Metal-Organic-Framework Nanosheets Used as Biomimetic Enzymes. *Adv. Mater.* **2016**, *28*, 4149−4155.

(28) Huang, Y.; Zhao, M.; Han, S.; Lai, Z.; Yang, J.; Tan, C.; Ma, Q.; Lu, Q.; Chen, J.; Zhang, X.; Zhang, Z.; Li, B.; Chen, B.; Zong, Y.; Zhang, H. Growth of Au Nanoparticles on 2D Metalloporphyrinic Metal-Organic Framework Nanosheets Used as Biomimetic Catalysts for Cascade Reactions. *Adv. Mater.* **2017**, *29*, 1700102.

(29) Sun, H.; Gao, N.; Dong, K.; Ren, J.; Qu, X. Graphene Quantum Dots-Band-Aids Used for Wound Disinfection. *ACS Nano* **2014**, *8*, 6202−6210.

(30) Shukla, A. K.; Sharma, C.; Acharya, A. Bioinspired Metal-Free Fluorescent Carbon Nanozyme with Dual Catalytic Activity to Confront Cellular Oxidative Damage. *ACS Appl. Mater. Interfaces* **2021**, *13*, 15040−15052.

(31) Liang, Q.; Xi, J.; Gao, X. J.; Zhang, R.; Yang, Y.; Gao, X.; Yan, X.; Gao, L.; Fan, K. A Metal-Free Nanozyme-Activated Prodrug Strategy for Targeted Tumor Catalytic Therapy. *Nano Today* **2020**, *35*, 100935.

(32) Zhang, L.; Zhang, L.; Deng, H.; Li, H.; Tang, W.; Guan, L.; Qiu, Y.; Donovan, M. J.; Chen, Z.; Tan, W. In vivo Activation of pH-Responsive Oxidase-Like Graphitic Nanozymes for Selective Killing of *Helicobacter pylori*. *Nat. Commun.* **2021**, *12*, 2002.

(33) Liang, M.; Yan, X. Nanozymes: From New Concepts, Mechanisms, and Standards to Applications. *Acc. Chem. Res.* **2019**, *52*, 2190−2200.

(34) Jiang, D.; Ni, D.; Rosenkrans, Z. T.; Huang, P.; Yan, X.; Cai, W. Nanozyme: New Horizons for Responsive Biomedical Applications. *Chem. Soc. Rev.* **2019**, *48*, 3683−3704.

(35) Chen, Q.; Liu, Y.; Liu, J.; Liu, J. Liposome-Boosted Peroxidase-Mimicking Nanozymes Breaking the pH Limit. *Chem. − Eur. J.* **2020**, *26*, 16659−16665.

(36) Qing, Z.; Bai, A.; Chen, L.; Xing, S.; Zou, Z.; Lei, Y.; Li, J.; Liu, J.; Yang, R. An Activatable Nanoenzyme Reactor for Co-Enhanced Chemodynamic and Starving Therapy against Tumor Hypoxia and Antioxidant Defense System. *CCS Chem.* **2020**, *3*, 1217−1230.

(37) Chong, Y.; Liu, Q.; Ge, C. Advances in Oxidase-Mimicking Nanozymes: Classification, Activity Regulation and Biomedical Applications. *Nano Today* **2021**, *37*, 101076.

(38) Sun, S.-K.; Wang, H.-F.; Yan, X.-P. Engineering Persistent Luminescence Nanoparticles for Biological Applications: From Biosensing/Bioimaging to Theranostics. *Acc. Chem. Res.* **2018**, *51*, 1131−1143.

(39) Li, Y.; Gecevicius, M.; Qiu, J. Long Persistent Phosphors-from Fundamentals to Applications. *Chem. Soc. Rev.* **2016**, *45*, 2090−2136.

(40) Li, Z.; Zhang, Y.; Wu, X.; Huang, L.; Li, D.; Fan, W.; Han, G. Direct Aqueous-Phase Synthesis of Sub-10 nm "Luminous Pearls" with Enhanced in vivo Renewable Near-Infrared Persistent Luminescence. *J. Am. Chem. Soc.* **2015**, *137*, 5304−5307.

(41) Wu, S.; Chi, C.; Yang, C.; Yan, X. Penetrating Peptide-Bioconjugated Persistent Nanophosphors for Long-Term Tracking of Adipose-Derived Stem Cells with Superior Signal-to-Noise Ratio. *Anal. Chem.* **2016**, *88*, 4114−4121.

(42) Pan, Z.; Lu, Y.-Y.; Liu, F. Sunlight-activated Long-Persistent Luminescence in the Near-Infrared from Cr^{3+}-Doped Zinc Gallogermanates. *Nat. Mater.* **2012**, *11*, 58−63.

(43) Yan, L.-X.; Chen, L.-J.; Zhao, X.; Yan, X.-P. pH Switchable Nanoplatform for in vivo Persistent Luminescence Imaging and

Precise Photothermal Therapy of Bacterial Infection. *Adv. Funct. Mater.* **2020**, *30*, 1909042.

(44) Kalantari, M.; Ghosh, T.; Liu, Y.; Zhang, J.; Zou, J.; Lei, C.; Yu, C. Highly Thiolated Dendritic Mesoporous Silica Nanoparticles with High-Content Gold as Nanozymes: The Nano-gold Size Matters. *ACS Appl. Mater. Interfaces* **2019**, *11*, 13264−13272.

(45) McNally, R. The United States Pharmacopoeia, 24th Revision. *The United States Pharmacopeial Convention*; 2000, Appendix 77.

(46) Wang, Z.; Upputuri, P. K.; Zhen, X.; Zhang, R.; Jiang, Y.; Ai, X.; Zhang, Z.; Hu, M.; Meng, Z.; Lu, Y.; Zheng, Y.; Pu, K.; Pramanik, M.; Xing, B. pH-Sensitive and Biodegradable Charge-Transfer Nano-complex for Second Near-infrared Photoacoustic Tumor Imaging. *Nano Res.* **2019**, *12*, 49−55.

(47) Zhao, H.; Joseph, J.; Fales, H. M.; Sokoloski, E. A.; Levine, R. L.; Vasquez-Vivar, J.; Kalyanaraman, B. Detection and Character-ization of the Product of Hydroethidine and Intracellular Superoxide by HPLC and Limitations of Fluorescence. *Proc. Natl. Acad. Sci. U. S. A.* **2005**, *102*, 5727−5732.

(48) Jv, Y.; Li, B.; Cao, R. Positively-charged Gold Nanoparticles as Peroxidiase Mimic and Their Application in Hydrogen Peroxide and Glucose Detection. *Chem. Commun.* **2010**, *46*, 8017−8019.

(49) Ge, S.; Liu, F.; Liu, W.; Yan, M.; Song, X.; Yu, J. Colorimetric Assay of K-562 Cells Based on Folic Acid-conjugated Porous Bimetallic Pd@Au Nanoparticles for Point-of-Care Testing. *Chem. Commun.* **2014**, *50*, 475−477.

(50) Thamphiwatana, S.; Gao, W.; Obonyo, M.; Zhang, L. In Vivo Treatment of *Helicobacter pylori* Infection with Liposomal Linolenic Acid Reduces Colonization and Ameliorates Inflammation. *Proc. Natl. Acad. Sci. U. S. A.* **2014**, *111*, 17600−17605.

(51) Wang, J.; Ma, Q.; Hu, X.-X.; Liu, H.; Zheng, W.; Chen, X.; Yuan, Q.; Tan, W. Autofluorescence-Free Targeted Tumor Imaging Based on Luminous Nanoparticles with Composition-Dependent Size and Persistent Luminescence. *ACS Nano* **2017**, *11*, 8010−8017.

(52) Stefka, A. T.; Feehley, T.; Tripathi, P.; Qiu, J.; McCoy, K.; Mazmanian, S. K.; Tjota, M. Y.; Seo, G. Y.; Cao, S.; Theriault, B. R.; Antonopoulos, D. A.; Zhou, L.; Chang, E. B.; Fu, Y.-X.; Nagler, C. R. Commensal Bacteria Protect against Food Allergen Sensitization. *Proc. Natl. Acad. Sci. U. S. A.* **2014**, *111*, 13145−13150.

(53) Buffie, C. G.; Jarchum, I.; Equinda, M.; Lipuma, L.; Gobourne, A.; Viale, A.; Ubeda, C.; Xavier, J.; Pamer, E. G. Profound Alterations of Intestinal Microbiota Following a Single Dose of Clindamycin Results in Sustained Susceptibility to Clostridium Difficile-Induced Colitis. *Infect. Immun.* **2012**, *80*, 62−73.